Riemannian classification of single-trial surface EEG and sources during checkerboard and navigational images in humans

Cédric Simar[2], Nichita Bozga[2], Robin Petit[2,4], Axelle Leroy[1], Ana-Maria Cebolla[1], Mathieu Petieau[1], Gianluca Bontempi[2], and Guy Cheron[1,3]

1. Lab. Neurophysiology and Movement Biomechanics, Neuroscience Institute, Université Libre de Bruxelles (ULB), Brussels, Belgium

2. Machine Learning Group, Computer Science Department, Faculty of Sciences, Université Libre de Bruxelles (ULB), Brussels, Belgium

3. Lab. Electrophysiology, Université de Mons-Hainaut, Mons, Belgium

4. Interuniversity Institute of Bioinformatics in Brussels, Université Libre de Bruxelles-Vrije Universiteit Brussel, Brussels, Belgium

Author to whom correspondence should be addressed; Cédric Simar; e-mail: cedric.simar@ulb.be

Abstract

Objective. Different visual stimuli are classically used for triggering visual evoked potentials comprising well-defined components linked to the content of the displayed image. These evoked components result from the average of ongoing EEG signals in which additive and oscillatory mechanisms contribute to the component morphology. The evoked related potentials often resulted from a mixed situation (power variation and phase-locking) making basic and clinical interpretations difficult. Besides, the grand average methodology produced artificial constructs that do not reflect individual peculiarities. This motivated new approaches based on single-trial analysis as recently used in the brain-computer interface field.

Approach. We hypothesize that EEG signals may include specific information about the visual features of the displayed image and that such distinctive traits can be identified by state-of-the-art classification algorithms based on Riemannian geometry. The same classification algorithms are also applied to the dipole sources estimated by sLORETA.

Main results and significance. We show that our classification pipeline can effectively discriminate between the display of different visual items (Checkerboard versus 3D navigational image) in single EEG trials throughout multiple subjects. The present methodology reaches a single-trial classification accuracy of about 84% and 93% for inter-subject and intra-subject classification respectively using surface EEG. Interestingly, we note that the classification algorithms trained on sLORETA sources estimation fail to generalize among multiple subjects (68%), which may be due to either the average head model used by sLORETA or the subsequent spatial filtering failing to extract discriminative information, but reach an intra-subject classification accuracy of 86%.

1. Introduction

Visual evoked potentials are often used to better understand the EEG contribution to the successive processing stages of visual inputs, which generate the well-defined components of the evoked potentials. These evoked potentials may be triggered by the display of different sorts of visual stimuli from simple (e.g. checkerboard) [1]–[3] to more complex ones (e.g. human face, 3D or moving image) [2], [4]–[8]. They are obtained by the average of numerous trials of ongoing EEG signals resulting in well-designed and easily recognizable event-related potentials (ERP). However, these evoked responses result from at least two different mechanisms sustained by the additive or the oscillation models [9]–[13]. For the additive model, the evoked responses result from sequential bottom-up processing of sensory inputs. This produces a specific sequence of monophasic evoked component peaks that are originally embedded in spontaneous EEG background. This latter EEG activity is considered as noise ruled out by the subsequent averaging. For the oscillatory model, the evoked potential might result from phase-locking of the ongoing EEG rhythms within specific frequency bands. This EEG phase reorganization can be measured by the inter-trials coherency (ITC), as a response to the external stimulation. On the fundamental level, this measure is interesting only when there are no simultaneous variations (increase or decrease) of the related EEG powers. In this case, we are in presence of a pure phase-locking and the evoked responses are only due to a reorganization of the ongoing EEG oscillation. For example, this is the case of the N30 component of the somatosensory evoked potential for which 70% of amplitude is due to pure phase locking [14]. The fact that, in the majority of ERP studies, a mixed situation (power variation and phase-locking) occurs, makes basic and clinical interpretations difficult. Another disadvantage originates from the fact that, in the majority of evoked potentials studies, a grand average among a cohort of patients is performed. Although the grand average method allows appropriate statistics [15] and practical conclusions about basic or clinical outcomes, it masks the individual peculiarities which may be critical from a clinical point of view. This problem is particularly crucial when diagnosis tools are based on grand average evoked potentials [16]. Similarly, the application of inverse modeling [17], [18] applied to grand average data provides very efficient recognition of the ERP generators [7], [19]–[21] but does not facilitate the determination of individual characteristics. In the face of these shortcomings of classical ERP analysis, the introduction of machine learning tools based on different classification pipelines such as Riemannian geometry may allow better exploitation of single trials and individual characteristics in the evoked potentials domain [22]–[31].

We hypothesize that the aforementioned ERP components of the EEG signals contain discriminative information characterizing the visual features of the image that can be identified by a state-of-the-art classification pipeline based on the canonical Riemannian geometry of covariance matrices. In this work, we use a classification pipeline based on xDAWN spatial filtering [23] and Riemannian geometry applied on raw EEG trials recorded during visual stimulation. Riemannian geometry classifiers have received growing attention in the last few years [32], particularly due to their first-class performance in international Brain-Computer Interface (BCI) competitions [33]. Besides, special attention is given to the potential advantage of introducing inverse modeling to the Riemannian classification pipeline.

We show that our present methodology can effectively discriminate between single-trial EEG signals from different visual items presentation (Checkerboard versus 3D navigational image) with a classification accuracy of about 84% and 93% for the inter-subject and intra-subject condition respectively. These successful results motivate us to introduce the "Riemannian Single-Trial Analysis" (RSTA) approach, which interest will be further discussed in comparison to the Grand Average Analysis approach commonly used in neuroscience.

2. Materials and methods

2.1 Participants

The data was collected from 15 healthy volunteers. All participants were right-handed, had no neurological condition, and normal vision, including 3D vision. Each participant gave informed consent to the experimental procedures. All experimental protocols were approved by the Ethic comity of Université Libre de Bruxelles, CHU Brugmann, and conducted in conformity with the European Union directive 2001/20/EC of the European Parliament.

2.2 Experimental paradigms

Participants were watching the EGA screen of an IBM Laptop (screen of 22.0 cm height, 30.3 cm width; refresh rate of 75 Hz, resolution of 800 x 600 pixels) centered on the line of gaze at a distance of 30 cm from the eyes through a cylindrical tunnel adapted to remove any external visual interferences, as previously used by our group [7]. We presented a sequence of checkerboard comprising 96 images intermixed with 96 grey images and a sequence of 3D-Tunnel presentations containing 192 images from four randomized corridor directions (up, down, right, and left) giving an implicit illusion of virtual navigation intermixed with grey images (Figure 1).

2.3 Stimulation and recording parameters

All participants performed passive observation of the aforementioned visual stimuli. The Checkerboard pattern and the 3D-Tunnel were alternatively presented with a uniform grey image (Figure 1A, B). An identical stimulation rate (1.0 Hz) was used in both conditions. Checkerboard stimulus consisted of black and white rectangles (4.5 x 4.0 cm) alternating 96 times with the grey page, which corresponded to full-contrast black and white squares (black field 15 lx; white field 101 lx).
The grey page luminance was about 43 lx. The 3D-Tunnel was non-stereoscopic but included perspective cues generated by the OpenGL graphic libraries [34] (Figure 1A, B). It represented a tunnel with stone-textured walls (stone dimension 1.25 cm^2 at the periphery to 0.15 cm^2 close to the center) in the form of a pipe with a constant circular cross-section. These different stimuli with a pattern contrast of about 50 % display subtended 7°(w) × 5° (h) at the eye. Thus, both foveal and parafoveal retinal fields were stimulated. The luminance of the tunnel evolved from 39 lx at the periphery to 74 lx close to the center. The presentation of each visual item

(presentation time of 500 ms) was immediately followed by the presentation of a uniform grey image (also for 500 ms).
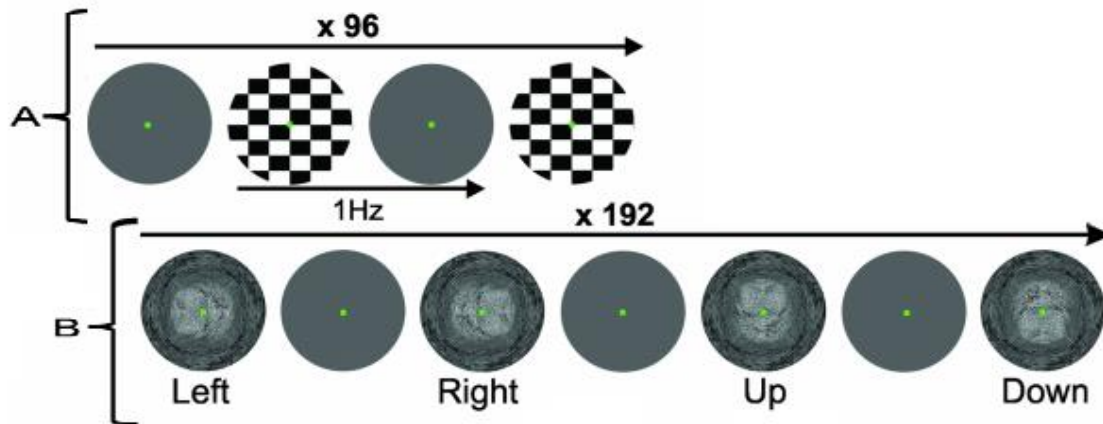

Figure 1. (**A, B**) *Overview of the two different stimulation paradigms. A: paradigm 1, Checkerboard images (upper line) followed by grey screens. B: paradigm 2, 3D Tunnels randomly presented in the 4 directions (up, down, left, right), followed each time by a grey screen.*

2.4 EEG data treatment and event-related potentials

EEG data were recorded with an active-shield cap using 128 Ag / AgCl sintered ring electrodes and shielded co-axial cables (5–10 electrode system placements) comfortably adjusted to the participant's head. All recordings were referenced to the left earlobe electrode. Vertical and horizontal eye movements (EOG) were recorded bipolarly. All electrode impedances were maintained below 5kΩ. Scalp potentials were amplified by ANT DC-amplifiers (ANT neuro system, the Netherlands) and digitized at a rate of 2.048 Hz using a resolution of 16 bit (range 11 mV). A band-pass filter from DC to 256 Hz and a notch filter (47.5 - 52.5 Hz) were also applied. Participants were asked to avoid eye blinks and to focus on the green dot presented in the middle of the screen to reduce eye artifacts. In order to verify the effectiveness of the eye fixation requirement, the number of eye movements was recorded throughout the different visual stimulation periods. For this, saccades including small saccades of about 0.8° and other eye movements were automatically selected by a Matlab (MathWorks Inc) script using eye velocity threshold. This selection was then verified by visual inspection. For all subjects, the fixation requirement was respected. Only 0.19 ± 0.09 saccades per second were recorded, irrespective of the type of image presented to the participant. Off-line data treatment and statistics were performed using EEGLAB software [35]. Artifactual portions of the EEG data were rejected after appropriate independent component analysis (ICA). Eventually, a zero-phase IIR bandpass filter with cut-off frequencies at 1 Hz and 45 Hz was applied and epochs containing samples from 1,000 ms before and 2,000 ms after the stimulus were extracted. More details about the EEG data processing can be found in our previous study [7].

Besides, in order to facilitate future applications in clinical routines, only the following 12 electrodes uniformly distributed on the scalp have been used for classification: F3, Fz, F4, C3, Cz, C4, P3, Pz, P4, O1, Oz, and O2.

2.5 XDAWN filtering and Covariances

As described in Barachant (2014) [36], the xDAWN algorithm estimates a chosen number of spatial filters that enhance the signal to noise ratio of the evoked potentials for each class. Let $E \in \mathbb{N}$ denote the number of electrodes, $X_i \in \mathbb{R}^{E \times T}$ denote the trial of index i with $1 \le i \le N^{(k)}$, T the number of time samples, and $N^{(k)}$ the number of trials from class k. Let $P^{(k)} \in \mathbb{R}^{E \times T}$ denote the average trial of class k, defined as:

$$P^{(k)} = \frac{1}{N^{(k)}} \sum_{i=0}^{N^{(k)}} X_i \qquad (1)$$

Let X denote the matrix representing the entire signal, obtained by concatenating all the trials from the two classes.

Each spatial filter is a vector $w \in \mathbb{R}^{E \times 1}$ and is estimated to increase the signal-to-noise ratio of its related class. In other words, for class k we have:

$$w^* = \underset{w}{\mathrm{argmax}} \ \frac{w^{\top} P^{(k)} P^{(k)^{\top}} w}{w^{\top} X X^{\top} w} \qquad (2)$$

These filters can be found by maximizing a generalized Rayleigh quotient, i.e. by solving the generalized eigenvalue problem on the matrices $P^{(k)} P^{(k)^{\top}}$ and $XX^{\top}$. Only the filters associated with the F highest eigenvalues are selected (F being the parameterizable number of xDAWN spatial filters).

Let $W^{(k)} \in \mathbb{R}^{E \times F}$ denote the selected spatial filters for class k, and $W = \left[W^{(0)}, W^{(1)} \right] \in \mathbb{R}^{E \times 2F}$ the aggregation of the spatial filters. The spatially filtered data is then defined by $Z_i \in \mathbb{R}^{E \times 2F}$:

$$Z_i = W^{\top} X_i \qquad (3)$$

We define a new matrix $\tilde{Z}_i \in \mathbb{R}^{4F \times T}$ by concatenating the filtered averaged trials from both classes (0 and 1) with the spatially filtered data as follows:

$$\tilde{Z}_i = \begin{bmatrix} W^{(0)^{\top}} P^{(0)} \\ W^{(1)^{\top}} P^{(1)} \\ Z_i \end{bmatrix} \qquad (4)$$

Finally, we can estimate the covariance matrix $\Sigma_i \in \mathbb{R}^{4F \times 4F}$ of $\tilde{Z}_i$:

$$\Sigma_i = \frac{1}{N} \tilde{Z}_i \tilde{Z}_i^{T} \qquad (5)$$

In particular, the shape of covariance matrices estimated after filtering the data is $4F \times 4F$. In order to main covariance matrices of shape 12×12, we fixed the number of filters $F = 3$.

In practice, Σ_i is computed using a well-conditioned estimator such as Ledoit-Wolf [37] or OAS [38].

2.6 Tangent space mapping

In all our classification pipelines, we apply a tangent space mapping operator to the previously estimated covariance matrices and use the mapped result as the input to a logistic regression classifier.

Covariance matrices are symmetric positive definite (SPD) and therefore do not lie in a vector space but in a convex cone [39] which has a Riemannian manifold structure, i.e. for each point of the manifold, there is an associated tangent space where a dot product is defined. In particular, we consider the tangent space at the point Σ_{ref} which corresponds to the geometric mean of the whole set of covariance matrices. More specifically, Σ_{ref} is the point minimizing the average Fréchet distance to the set of covariance matrices. The choice of Σ_{ref} is motivated by the observation from Tuzel *et al.*, [40] that the geometric mean is the point where the mapping onto the tangent space leads to the best local approximation of the manifold.

Tangent space mapping is the action of projecting the SPD matrices from the manifold onto the associated tangent space. In the tangent space, the $n \times n$ covariance matrices will be represented by a vector of dimension $n(n + 1)/2$. This projection operator at the reference point Σ_{ref} is defined by Barachant *et al.*, [41] as the upper triangular matrix of $\sqrt{2}\,(1_E\,1_E^\top - I_E)\,\Phi(\Sigma)$ where $\Phi(\Sigma)$ is defined as:

$$\Phi(\Sigma) = \log_{\Sigma_{\mathrm{ref}}}(\Sigma) = \Sigma_{\mathrm{ref}}^{1/2} \log\!\left(\Sigma_{\mathrm{ref}}^{-1/2}\,\Sigma\,\Sigma_{\mathrm{ref}}^{-1/2}\right) \Sigma_{\mathrm{ref}}^{1/2} \tag{6}$$

where $\log_{\Sigma_{\mathrm{ref}}}(\Sigma)$ denotes the matrix logarithm of Σ with respect to Σ_{ref}.

2.7 Source analysis

The objective of source analysis is to improve spatial resolution, increase SNR, and detect subcortical activities not directly observable on scalp EEG. In this work, we estimated cortical and subcortical sources using the non-parametric inverse method Standardized Low Resolution Electromagnetic Tomography (sLORETA) [17], [42]. This work used the sLORETA estimation implemented in the MNE Python library [43] and which is formally defined as follows. Let $\hat{J}(\alpha) \in \mathbb{R}^{3M \times T}$ be the source estimation matrix:

$$\hat{J}(\alpha) = T(\alpha)X := K^\top (KK^\top + \alpha I)^{-1}X,$$

where $E \in \mathbb{N}$ is the number of electrodes at the scalp surface, $M \in \mathbb{N}$ is the number of sources within the brain volume, $X \in \mathbb{R}^{E \times T}$ is the EEG signal matrix, $K \in \mathbb{R}^{E \times 3M}$ is the lead filed matrix and $\alpha > 0$ is a regularization parameter.

Consider $\Sigma\left(\hat{J}(\alpha)\right)$, the covariance matrix of $\hat{J}(\alpha)$ defined as:

$$\Sigma\left(\hat{J}(\alpha)\right) = \Sigma(T(\alpha)X) = T(\alpha)\Sigma(X)T(\alpha)^\top = K^\top(KK^\top + \alpha I)^{-1}K.$$

$\Sigma\left(\hat{J}(\alpha)\right)$ is a $3M \times 3M$ square matrix with M diagonal blocks of shape 3×3 denoted by $\Sigma_1, \dots, \Sigma_M$. The normalized sLORETA source estimation of the voxel ℓ is therefore given by:

$$\hat{J}_{\text{sLORETA}}(\alpha)_\ell := \Sigma_\ell^{-1/2}\,\hat{J}(\alpha)_\ell = \Sigma_\ell^{-1/2}\,T(\alpha)_\ell\,X \in \mathbb{R}^{3\times T}$$

where $T(\alpha)_\ell$ is the ℓth $3 \times E$ row block of $T(\alpha)$.

2.8 Classification pipelines

This section describes the classification pipelines illustrated in Figure 2. The accuracy of each inter-subject pipeline was estimated using a Leave-One-Subject-Out Cross-Validation (LOSO-CV) where each subject out of the 15 has been used for the validation of the classification algorithm trained using the remaining 14 subjects. Similarly, the accuracy of each intra-subject pipeline was estimated using a 4-Fold Cross-Validation where a quarter of each subject trials were used for validation of the classification algorithm using the remaining three quarters. xDAWN spatial filters were estimated on the training set and applied on the validation set.

The classification pipeline of both inter-subject and intra-subject raw EEG signals from the 12 electrodes of either 3D Tunnel versus Checkerboard or 3D Tunnel grey versus Checkerboard grey without inverse modeling includes (i) xDAWN spatial filtering, (ii) the estimation of covariance matrices, (iii) the projection onto the tangent space (TS) and (iv) a logistic regression (LR) classifier.

The classification pipeline of both inter-subject and intra-subject EEG signals of 3D Tunnel versus Checkerboard with inverse modeling includes (i) the estimation of cortical sources based raw EEG signals using the Desikan-Killiany atlas [44], [45], (ii) the averaging of cortical sources activations per atlas region, (iii) xDAWN spatial filtering, (iv) the estimation of covariance matrices, (v) the projection onto the tangent space (TS) and (vi) a logistic regression (LR) classifier. In this case, xDAWN spatial filtering operates on the 75 averaged sources activations instead of the raw EEG signals from the 12 electrodes.
Since the dataset is not balanced (96 Checkerboard and related grey images versus 192 3D-Tunnel and related grey images), the results of the classification pipelines were reported using appropriate metrics such as ROC curves, Precision-Recall curves and the confusion matrices.
The main Python libraries used in these pipelines are MNE [43], [46], NumPy [47], SciPy [48], and scikit-learn [49].
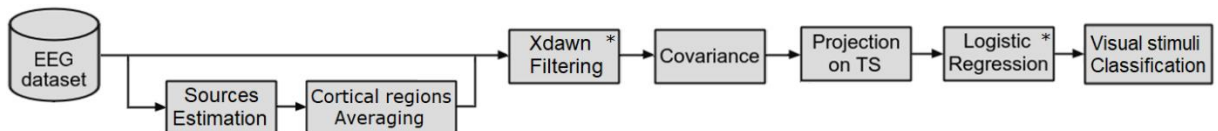

Figure 2. *Flow chart of the classification pipeline with and without inverse modeling. An asterisk in the upper-right corner denotes that the pipeline step is supervised.*

3 Results

3.1 ERP analysis

Figure 3 illustrates the grand average ERP differences observed between the different visual stimulations, highlighting the main characteristics of the early evoked components at around 100 ms (P100) for the Checkerboard (blue line) or the 3D Tunnel (red line) presentation. As previously observed by our group [7], the P100 component evoked by the Checkerboard was of higher amplitude than the P100 evoked by the 3D Tunnel, which presented a biphasic configuration during the time of the monophasic classical P100 related to the Checkerboard. These earlier evoked components were followed by a P220 in the EEG signals of Tunnels and Checkerboards but not in the signals of grey images, which only presented an early P100 and a small N140.
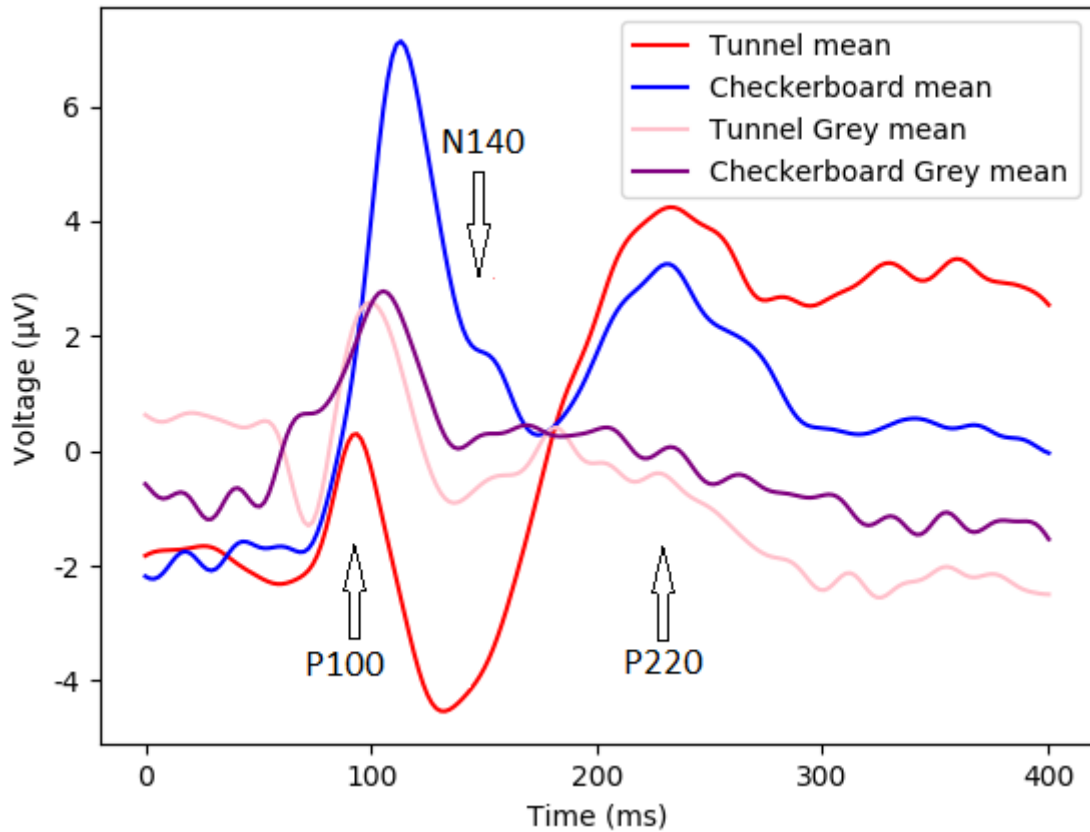

Figure 3. *Grand averaged event-related potential recorded on the occipital area (electrode Oz) corresponding to the 4 visual conditions: the Checkerboard (blue line), the 3D Tunnel (red line), the grey image following the Checkerboard (violet line), and the grey image following the 3D Tunnel (pink line). The arrows point to the P100, N140, and P220 components. The grand-averaged signal of each class k refers to the row corresponding to the Oz electrode of the matrix $P^{(k)}$ as defined in Equation 1.*

The visual distinction between the Tunnel and Checkerboard conditions disappeared when randomly chosen single trials originating from all subjects were superimposed (Figure 4A). This figure illustrates the fact that the discrimination was not possible by human visual inspection and is well representative of the difficulty of the classification task. When comparing the

superimposition of the single trials corresponding to the Tunnel and the Checkerboard (Figure 4A) with those corresponding to the Tunnel grey screens and the Checkerboard grey screens (Figure 4B), the visual discrimination of the latter conditions was even more difficult.
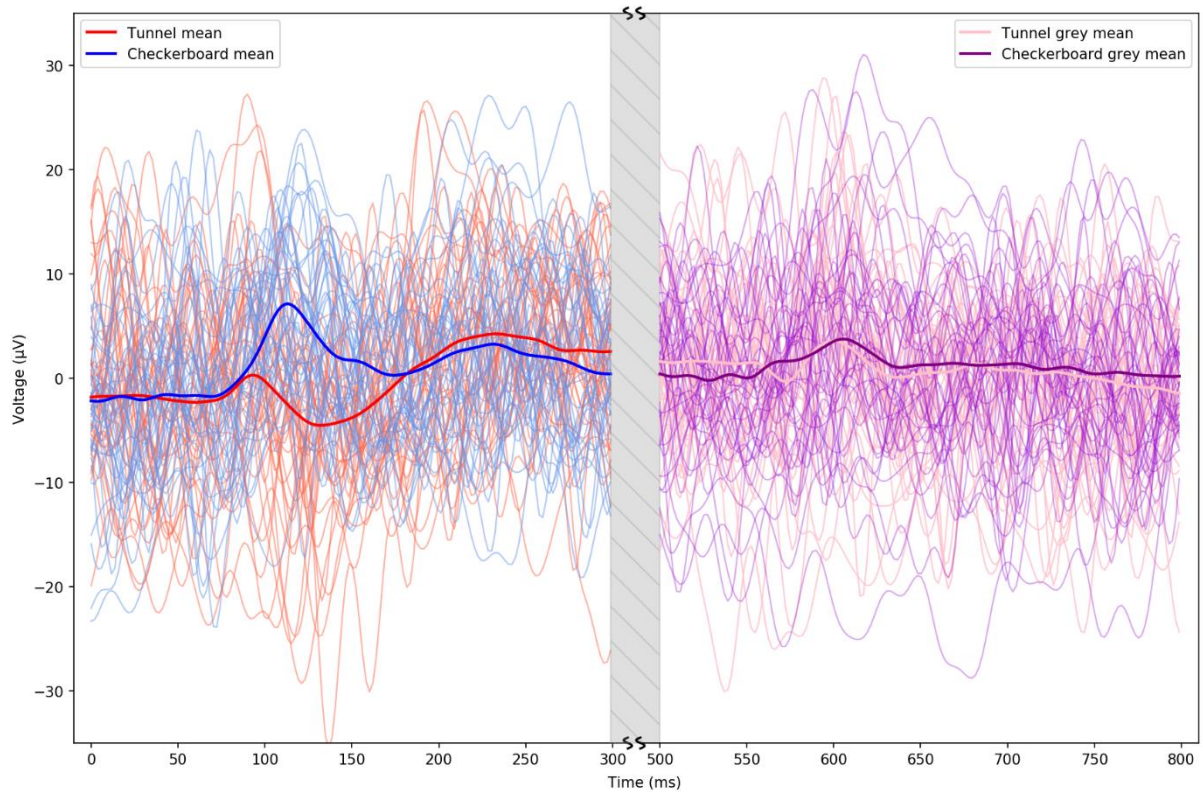

Figure 4. *(Left) Superimposition of single raw EEG signals recorded between 100 and 300 ms on electrode Oz from 40 randomly selected trials of Tunnel stimuli and 40 randomly selected trials of Checkerboard stimuli throughout all the subjects on which the grand average signals of all trials and all subjects corresponding to the Tunnel stimuli (red lines, n=2880 (192 trials x 15 subjects)) and the Checkerboard (blue lines, n=1440 (96 trials x 15 subjects)) are superimposed.*
*(**Right**) The same superimposition of single raw EEG signals recorded between 500 and 800 ms as in (left) are displayed for the Tunnel greys stimuli (pink lines, n=2880 (192 trials x 15 subjects)) and the Checkerboard greys (violet lines, n=1440 (96 trials x 15 subjects)).*

In contrast, when confronted with trials coming from a single subject, differences can be more visible to the human eye. For example, unlike in Figure 4 (left), in Figure 5 we can observe differences between the single trials of Tunnels and Checkerboards between 100 and 200 ms, with the Tunnels having a noticeably lower amplitude in the selected time limits. Therefore, we may expect higher accuracies from a classifier trained and evaluated with intra-subject EEG signals.
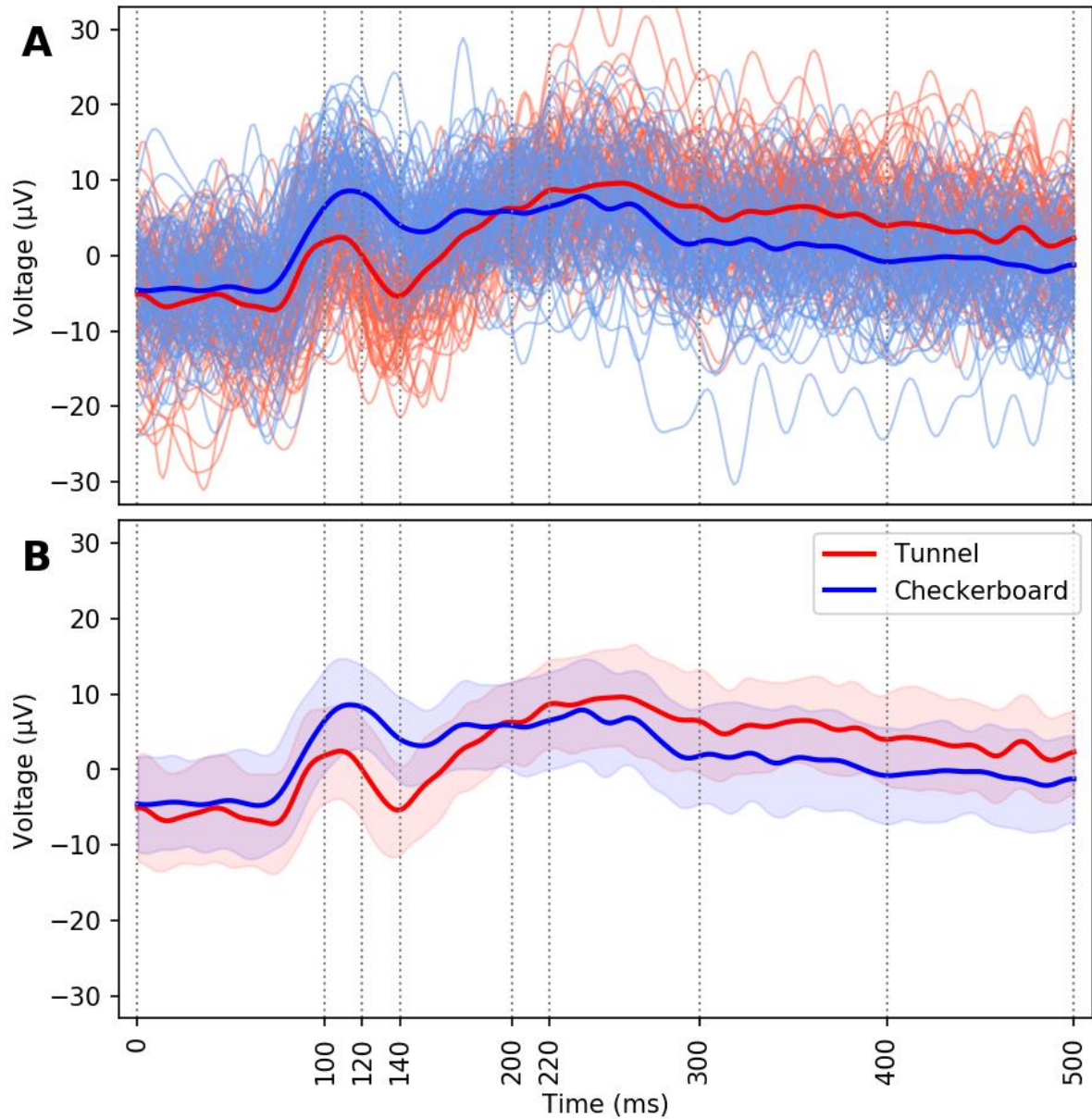
Figure 5. *(A) Superimposition of single raw EEG signals recorded on electrode Oz from all the trials of Tunnels and Checkerboards stimuli of one representative subject on which the grand average signals corresponding to the Tunnel (red lines, n=192) and the Checkerboard (blue lines, n=96) stimuli are superimposed. (B) Same grand average signals as in (A) with their respective standard deviation corresponding to the Tunnel (salmon area, n=192) and the Checkerboard stimuli (light blue area, n=96).*

3.2 Classification performance

3.2.1 Validation of the electrode selection

Prior to the main classification task, we first determined if sufficient discriminative information existed with regards to the number and localization of the 12 arbitrarily selected electrodes.

The number of electrodes was empirically validated by quantifying their impact on the classification accuracy using a forward feature selection method based on Riemannian geometry [50]. For this, we computed the distribution of classification accuracy with respect to the number of electrodes (Figure 6A) using a LOSO Cross-Validation. As a result, Figure 6A illustrates that the classification score for the Tunnel vs. Checkerboard reaches a global maximum using 9 electrodes, while the classification score for Grey Screens reaches its global maximum using all 12 electrodes.

Furthermore, in order to test which scalp region contains the most discriminative information, we used a triad of electrodes corresponding to the occipital, parietal, central, and frontal regions on which the classification pipeline was applied. Figure 6B illustrates this result for the Tunnel vs Checkerboard classification. The classification pipeline trained on the single trials of all subjects indistinctively reaches the best score for the occipital electrodes (75%), followed by the parietal electrodes (64%), and followed by the central and frontal electrodes (respectively 56% and 59%). In contrast, the same discriminative trend was not found for the classification of grey screens, where the occipital, parietal, central, and frontal zones scored respectively 54%, 56%, 54%, and 57%.
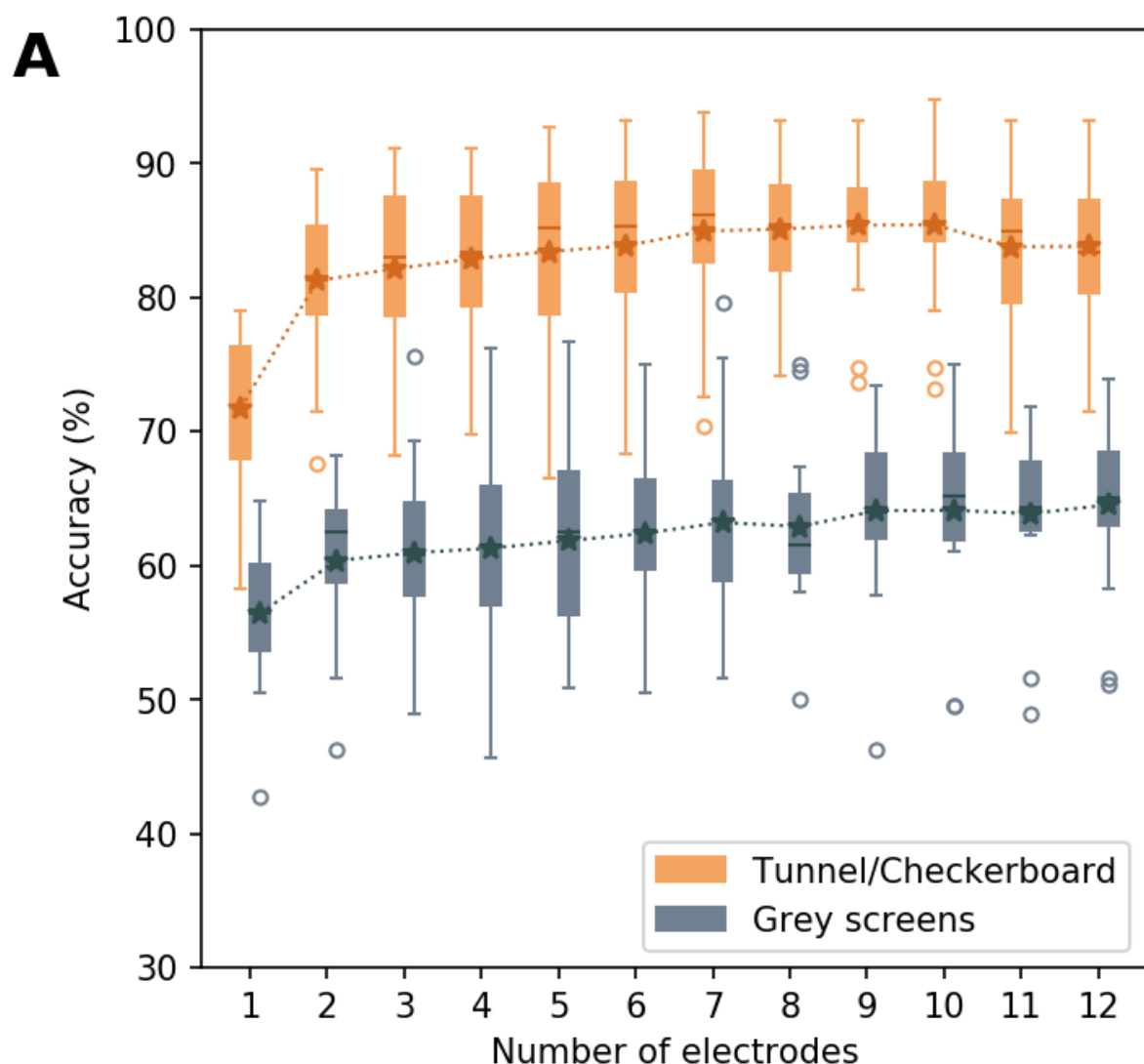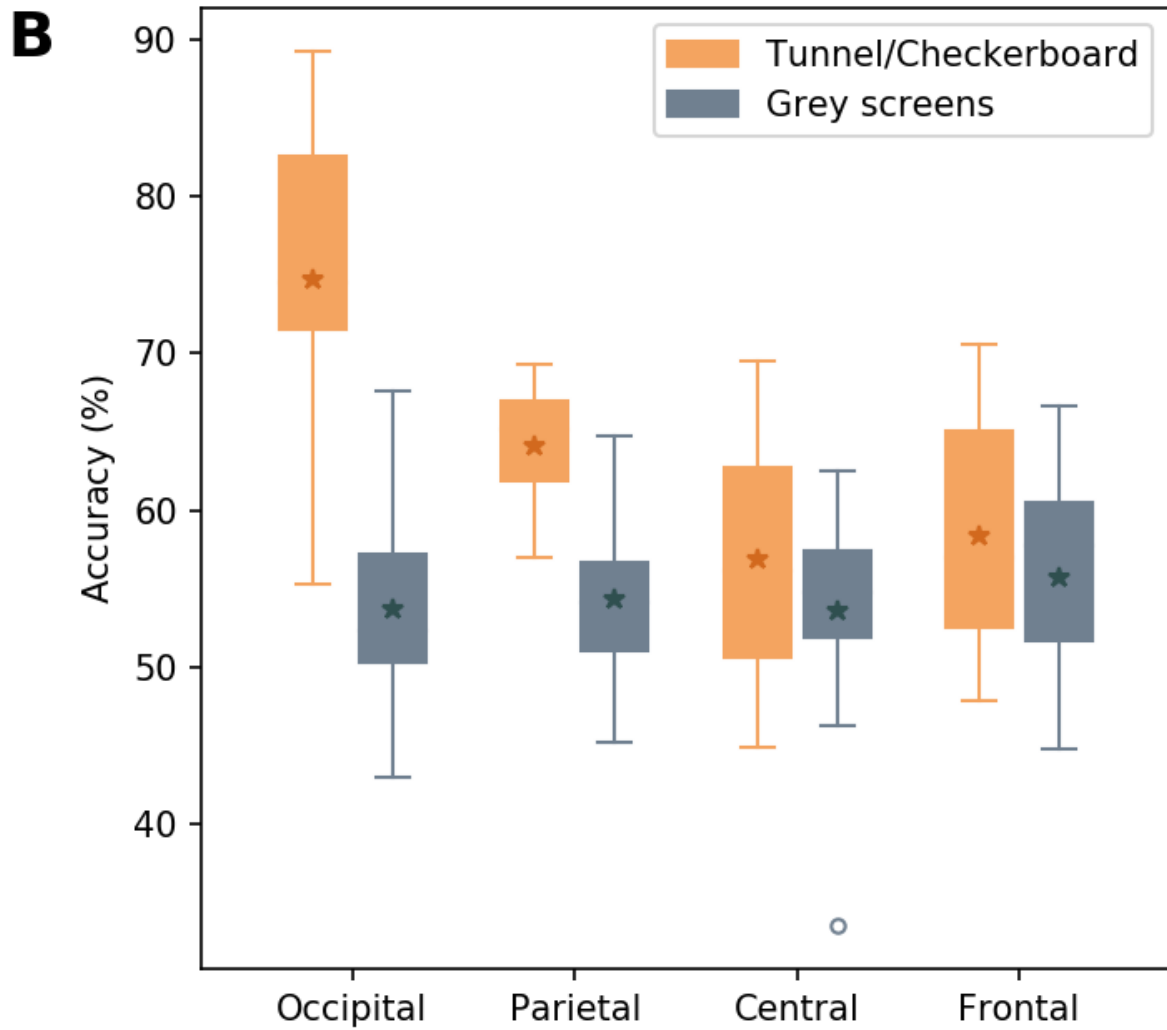
Figure 6. *Distribution of the Tunnel vs Checkerboard and Tunnel-Grey vs Checkerboard-Grey inter-subject cross-validated classification accuracy without inverse modeling with respect to the number of electrodes (**A**) and by scalp region (**B**) using only 3 electrodes from each locus (O1, O2, and Oz for the occipital locus, P3, P4, and Pz for the parietal locus, C3, C4, and Cz for the central locus, F3, F4 and Fz for the frontal locus).*

3.2.2 Inter-subject classification without inverse modeling

The main results of the classifications pipelines were illustrated by the ROC curve (along with the AUC), the Precision-Recall curve (along with the Average Precision), and the confusion matrix. Figure 7 illustrates these performance metrics computed on the results from the inter-subject classification pipelines without inverse modeling. The ROC curve for the Tunnel vs Checkerboard discrimination is more arched than the one for Grey Screens (Figure 7A), which is confirmed by the higher AUC of the first (0.92) compared to the latter (0.7). These results were further validated by the Precision-Recall curves (Figure 7B). Besides, the confusion matrices (Figure 7C) show a balanced recognition accuracy for Tunnels and Checkerboards, although both accuracies are significantly higher for the Tunnel vs Checkerboard (Figure 7C left) than the Grey Screens (Figure 7C right). The inter-subject Tunnel vs Checkerboard without

inverse modeling classifier and the inter-subject Grey Screens without inverse modeling classifier reached an accuracy of 84% and 64 % respectively.
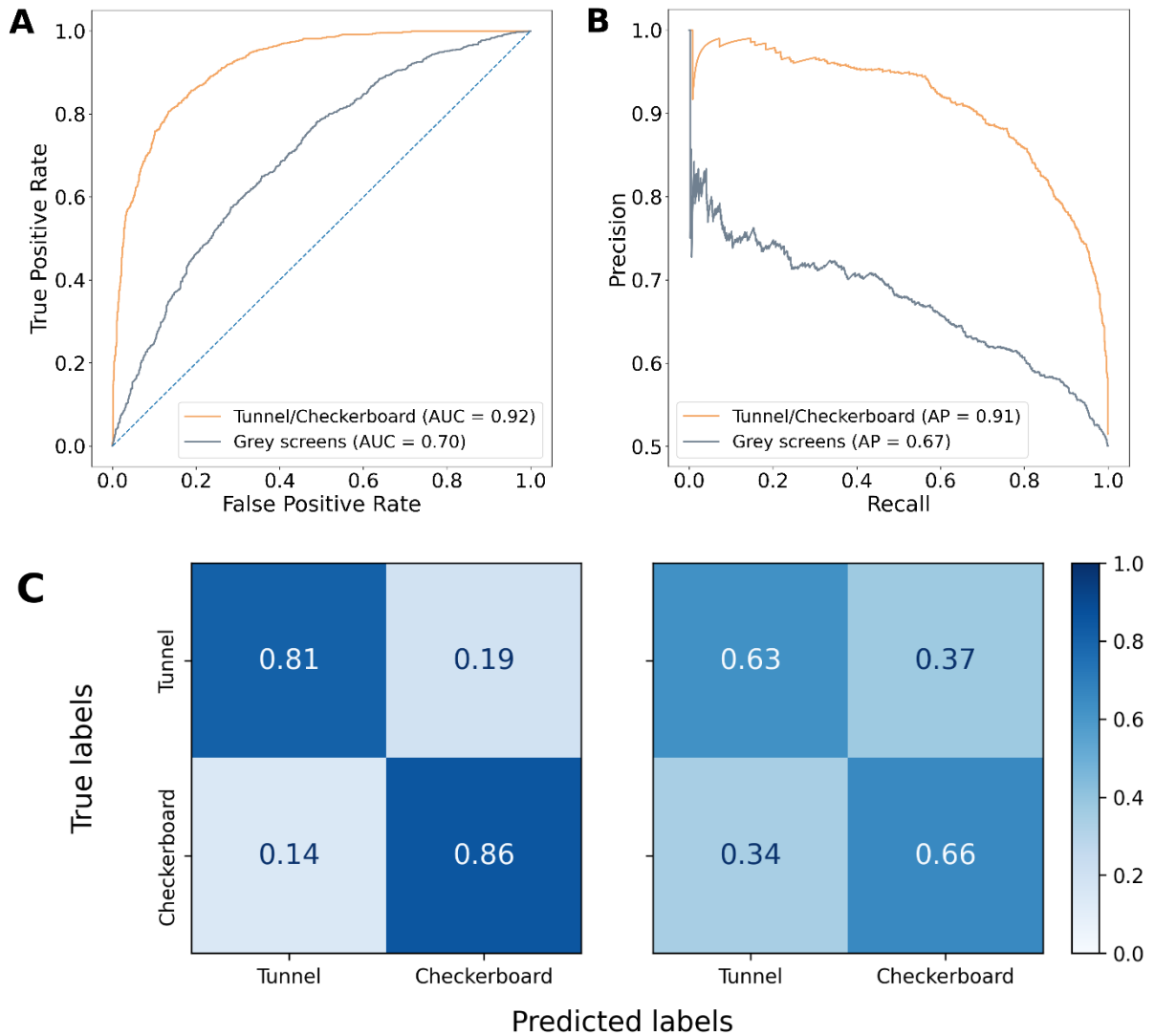

Figure 7. *ROC (**A**) and Precision-Recall (**B**) curves for the inter-subject classification of Tunnel vs Checkerboard and Grey Screens without inverse modeling. (**C**) Confusion matrices for the inter-subject classification of Tunnel vs Checkerboard (left) and Grey Screens (right) without inverse modeling.*

3.2.3   Intra-subject classification without inverse modeling

As expected, when trained on the same dataset, the intra-subject Tunnel vs Checkerboard and Grey Screens classification pipelines without inverse modeling reached higher accuracy scores than their inter-subject counterparts. We observed a classification accuracy of 93% and 81% for the discrimination of Tunnel vs Checkerboard and Grey Screens respectively, which corresponds to an increase of 9% and 17% from the inter-subject Tunnel vs Checkerboard and Grey Screens accuracy scores.

Figure 8 illustrates that the ROC curves (Figure 8A), the Precision-Recall curve (Figure 8B), and the confusion matrices (Figure 8C) confirmed the improved accuracy results. The ROC curve (Figure 8A) for the Tunnel vs Checkerboard discrimination task was more arched than that for the Grey Screens, which was confirmed by the higher AUC of the first (0.98) compared to the latter (0.89).
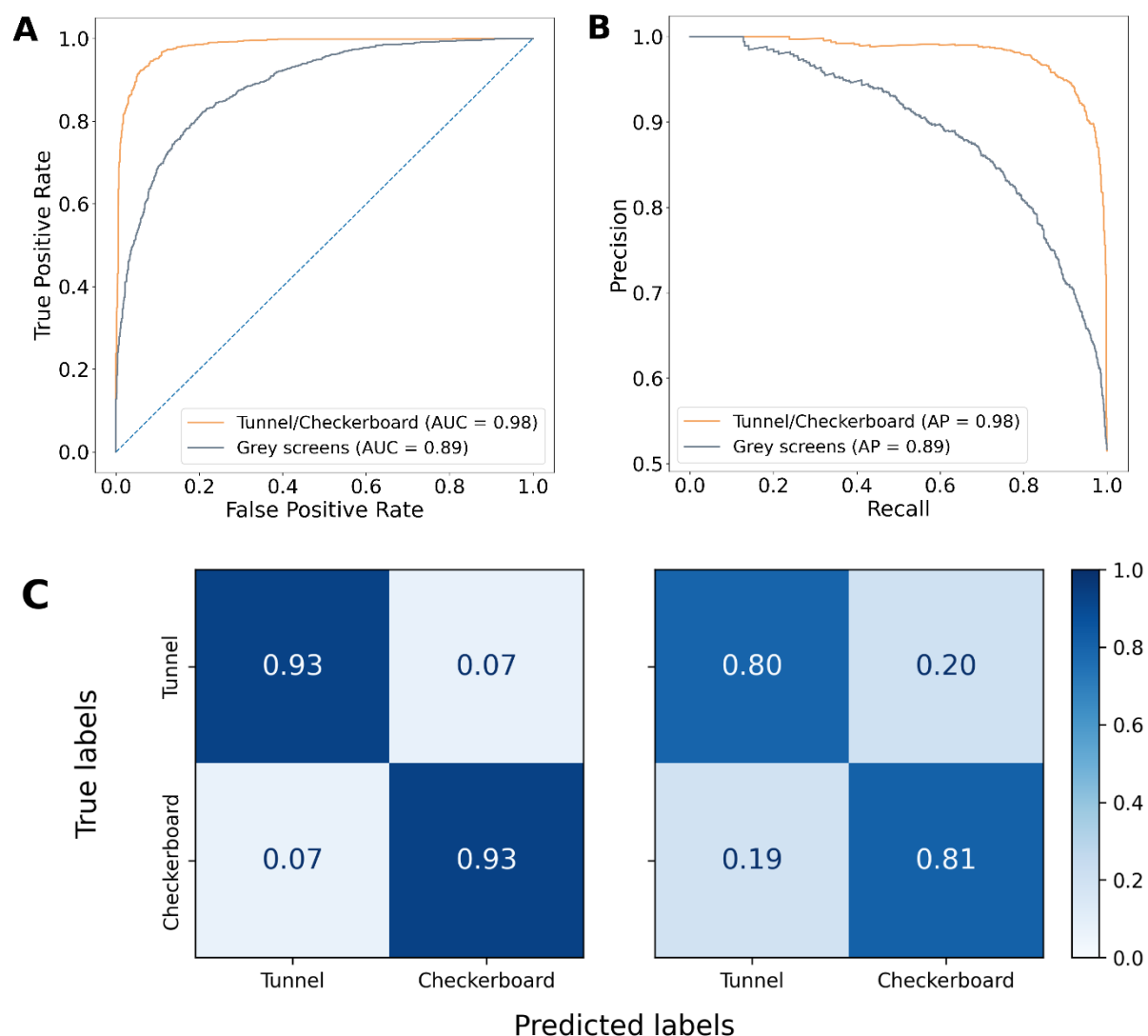

Figure 8. *ROC (**A**) and Precision-Recall (**B**) curves for the intra-subject classification of Tunnel vs Checkerboard and Grey Screens without inverse modeling. (**C**) Confusion matrices for the intra-subject classification of Tunnel vs Checkerboard (left) and Grey Screens (right) without inverse modeling.*

3.2.4 Inter-subject and intra-subject classification with inverse modeling

When working with inverse modeling on the discrimination of Tunnel vs Checkerboard, the inter-subject and intra-subject classification pipelines performed very differently on the same dataset. When applied to inter-subject data, the classification pipeline reached an accuracy of 68 %. However, the intra-subject approach has yielded significantly better results, reaching an accuracy of 86 %. The major differences in performances between the two classification tasks are illustrated in Figure 9, i.e. the shape of the ROC curves and their respective AUC (Figure 9A), the Precision-Recall curves (Figure 9B) as well as the confusion matrices (Figure 9C).
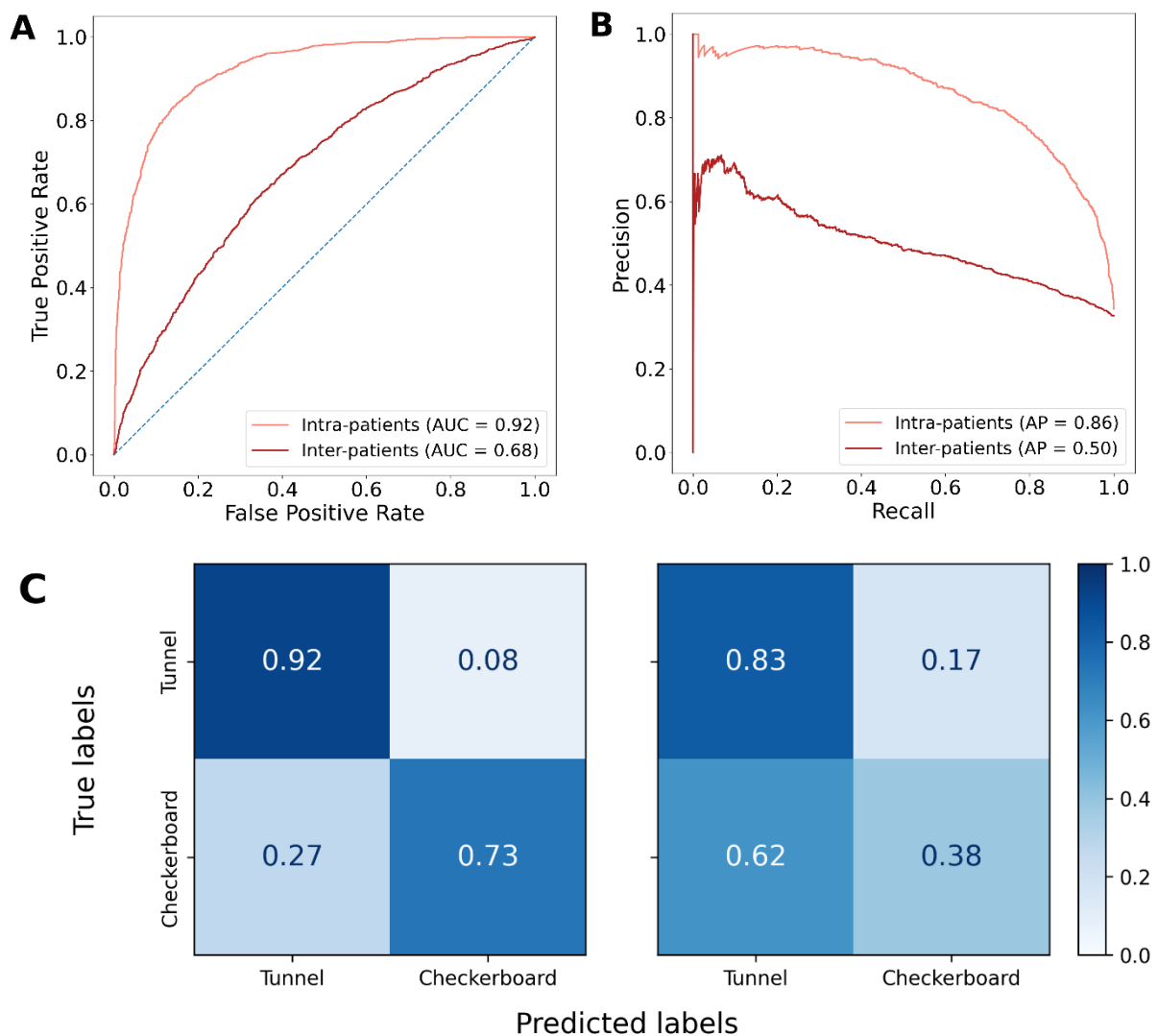

Figure 9. *ROC (A) and Precision-Recall (B) curves for the intra-subject and inter-subject classification of Tunnel vs Checkerboard with inverse modeling. (C) Confusion matrices for the intra-subject (left) and inter-subject (right) classification of Tunnel vs Checkerboard with inverse modeling.*

We further explored the intra-subject classification by exploring the sources activations of a representative subject around 140 and 220 ms. As illustrated in Figure 10A, B, sources activations seem to be higher during the visualization of the Tunnels than that of the Checkerboards. For the Tunnel, two main zones were highlighted (yellow), one in the occipital cortex and the other in the sensory-motor areas extending towards the frontal cortex. For the Checkerboard, the occipital region was also identified as well as the frontal cortex but less intensely. Although some subjects exhibited a less contrasting pattern as illustrated in Figure 10E, F, the differences remain in favor of higher cortical contribution for the Tunnel (occipital and frontal zones identified) while only the occipital region was identified for the Checkerboard. Figure 10C, F represents the activations of labeled cortical source areas as defined in the Desikan-Killiany atlas corresponding to the 3D brain visualizations from Figure 10A, B and D, E respectively. The highest sources were located in the cuneus (left and right hemispheres, respectively #7 and #8 of the Desikan-Killiany nomenclature), the lateral occipital zone (left #23 and right #24 hemispheres), and the peri-calcarine zone of the visual cortex (left #43 and right #44 hemispheres), during the observation of Tunnels.
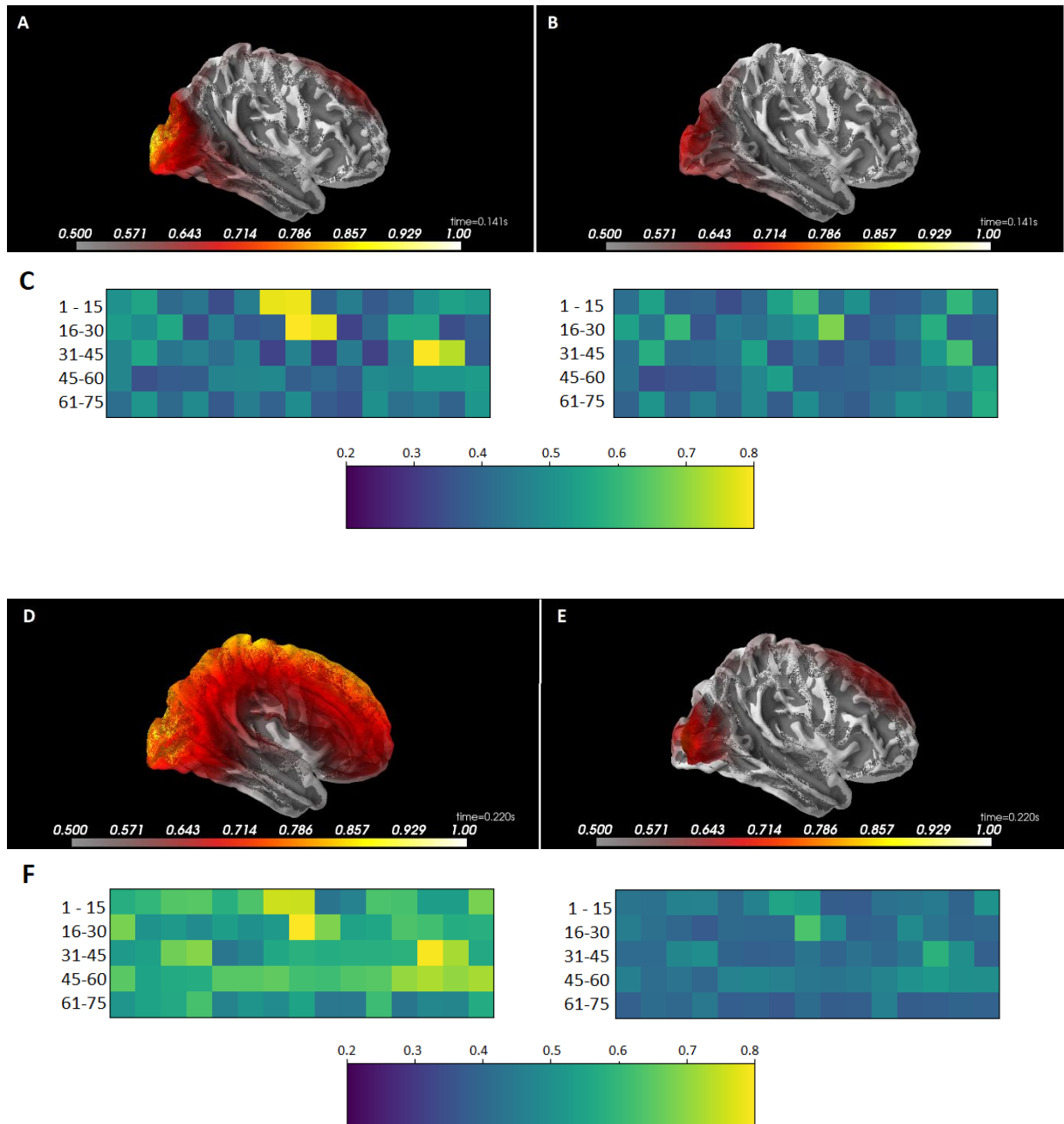
Figure 10. *Lateral view of the mean sources activations estimations (A, B, D, and E) and the corresponding matrix representation of the atlas regions (C and F) labeled as defined in the Desikan-Killiany atlas at two different times in a single representative subject; 140 ms (A and B) and 220 ms (D and E) after the stimuli, during the visualization of Tunnels (A and D) and Checkerboards (B and E). Sources activations are averaged from 10 milliseconds before to 10 milliseconds after the N140 (140 ms) and the P220 (220 ms) respectively.*

3.2.5 Summary of results

The boxplots in Figure 11 summarizes the comparative analysis of the classification pipelines with respect to the intra-subject or inter-subject conditions. The classification results for the intra-subject and inter-subject classification pipelines were computed using a 4-fold cross-validation and a Leave-One-Subject-Out Cross-Validation respectively. We observed that the accuracy for each classification task was significantly higher for the intra-subject compared to the inter-subject condition ($p < 0.001$). Additionally, we observed a statistical difference between the classification accuracy of the Tunnel vs Checkerboard with and without inverse modeling in the inter-subject condition ($p < 0.001$) but not in the intra-subject condition ($p > 0.01$). These statistical comparisons were computed using a Mann–Whitney U test. Besides, the classification performances for the Grey Screens Tunnel vs Checkerboard in the inter-subject and intra-subject conditions were statistically significantly higher than chance ($p < 0.001$). This latter statistical comparison was computed using a one sample Wilcoxon test.
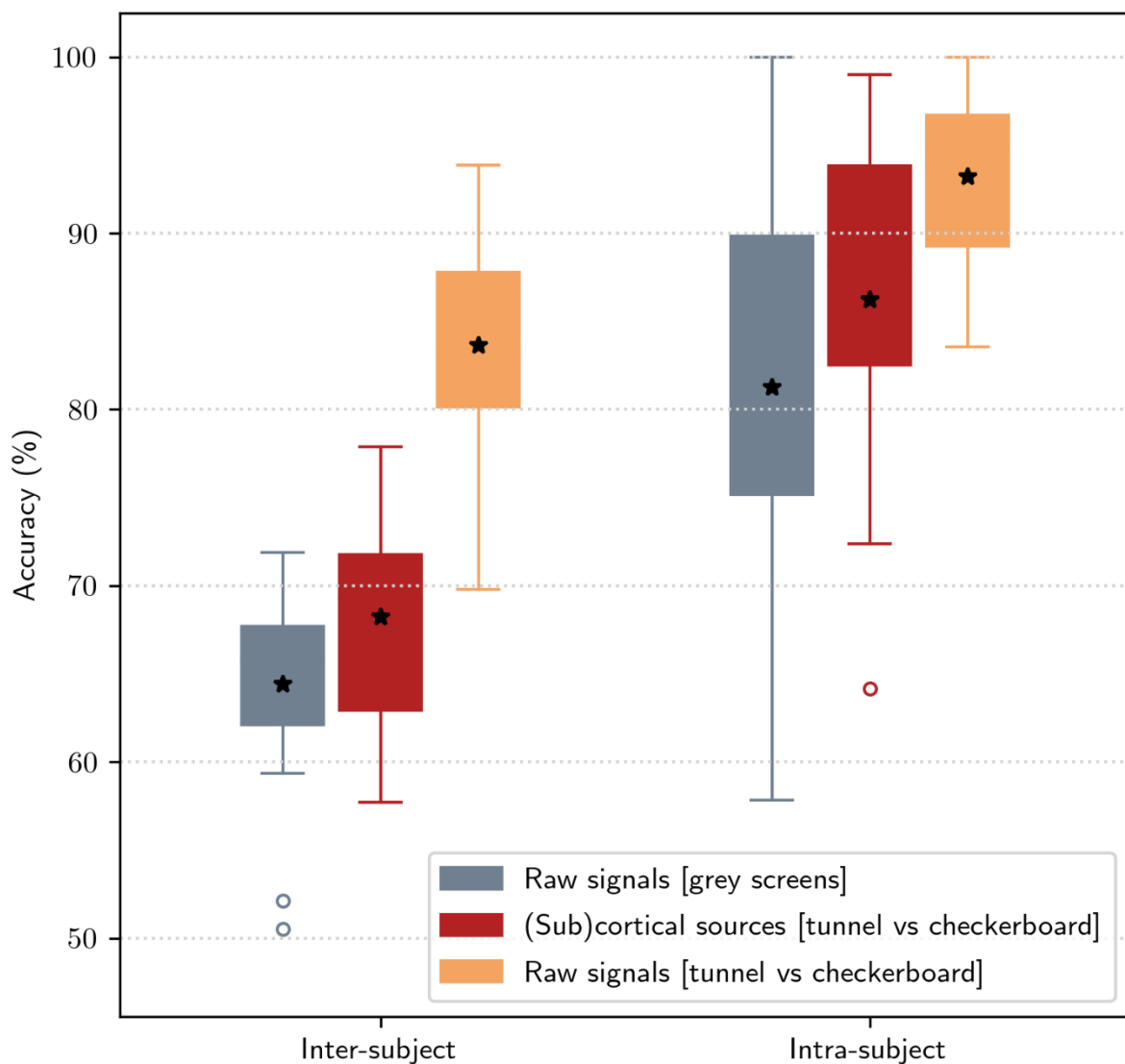

Figure 11. *Summary of the performances of the classification pipelines for inter-subject and intra-subject classification of raw signals from the Tunnel vs Checkerboard (light orange) and grey screens (grey) conditions, and of (sub)cortical sources from the Tunnel vs Checkerboard (red) condition.*

4 Discussion

In this work, we leveraged the BCI methodology and related mathematical tools in order to better analyze the EEG signals commonly summarized and interpreted by the analysis of the evoked potentials components. Since the renewing of the evoked potentials interpretation following the oscillation models by Makeig *et al.*, [9] and the introduction of EEGLab software [35], the dynamic aspects of the event-related potentials (ERP) contributed to better access to the underlying neurophysiological mechanisms sustaining the ERP components. At the same time, the development of the BCI domain [51], [52] necessitated online procedures in order to extract pertinent neural information from noisy environments. As BCI procedures are specifically devoted to work with only one subject at a time, the BCI tools are well appropriate to decipher individual EEG-evoked responses and to extend our understanding beyond grand average representations of the ERP.

We show that it is possible to effectively discriminate between the display of different visual items (Checkerboard versus 3D navigational image) in single related EEG signals corresponding to one subject. Besides, the present methodology allows us to demonstrate that the single-trial discrimination based on Riemannian classification pipelines can be generalized to multiple subjects constituting a single batch of single trials. In other words, we may here introduce the "Riemannian Single-Trial Analysis" (RSTA) approach, as opposed to the Grand Average Analysis (GAA) approach commonly used in clinical neuroscience. Although the latter is useful for highlighting statistically significant differences between subject populations, GAA is prone to capture artificial constructs due to individual peculiarities. Indeed, it is possible that averaged evoked components may be sign inverted or phase jittered depending on the subjects included in the grand average. Therefore, these statistically significant differences may be spurious and may not represent the underlying physiological characteristics of the observed evoked potential resulting from the GAA. Besides, a statistical difference induced by the GAA may not necessarily imply physiological plausibility nor genuine discriminative property that should be the basis of a clinical application. As opposed to the GAA, the objective of the RSTA approach is to allow, using interpretability techniques on Riemannian classification pipelines, the identification and extraction of subject, task, and trial-specific underlying discriminative patterns that can unlock a deeper understanding of the fundamental neurophysiological mechanisms.

It was previously shown in previous studies [53]–[57] that the single-trial configuration was able to discriminate cognitive evoked components, allowing the possibility to detect the intermittency of cognitive events during repetitive stimulation. Although the evoked components are not visually distinguishable in the present single-trial configuration, as displayed in Figure 4A, we show that our classification pipeline based on covariance matrices and Riemannian geometry is able to discriminate between the presentation of the two displays, reaching a single-trial classification accuracy of about 85% and 94% for inter-subject and intra-subject classification respectively.

Despite the methodological difference about the paradigm and the type of evoked potentials or brain signal recordings, the results of the present classification pipelines based on Riemannian geometry corroborate the single-trial classification performances of similar Riemannian approaches applied on objects familiarity recognition [58], motor imagery [59], [60], P300 BCI [61] and EEG respiratory states [62].

Using inverse modeling based on swLORETA [18], we previously showed that, whatever the presented image (Checkerboard or Tunnel), the same generators of the P100 were located in the occipital cortex (BA18 and BA19) and the right inferior temporal cortex (BA20). However, the left fusiform cortex (BA37) was additionally recruited only for the Checkerboard but not for the 3D Tunnel. In the present study, inverse modeling based on sLORETA mainly reproduces these results using the Desikan-Killiany atlas [44], [45] but the inter-subject classification pipeline based on sLORETA sources estimations reaches significantly lower accuracy when using estimated sources (68%) rather than raw EEG signals (84%). In contrast, the same classification method applied to intra-subject EEG reaches an accuracy and an AUC of 86% and 0.92 respectively. This performance is comparable to the intra-subject classification performances based on raw EEG signals (93%). The lower performance of inter-subject classification using sLORETA sources estimations may result from either (i) the morphological differences between the subject-specific cortical dipoles orientation and the average head model used to compute the sLORETA lead field matrix that may have blurred the signal differentiation between the two images or (ii) the subsequent xDAWN spatial filtering not being able to extract discriminative information that may be located in different, subject-specific, cortical atlas regions. Conversely, this problem does not occur when only one subject is considered. It is worth noting that the presentation of the grey image following a Checkerboard or a Tunnel induces a P135 occurring with common cerebellar and prefrontal generators (BA10) and distinctive cortical generators (the visual cortex (BA18) and the temporal cortex (BA20, BA21) for the Checkerboard and Tunnel image respectively). In this latter condition, our classification pipeline reaches performances statistically significantly higher than chance, reinforcing the idea that the contents of the grey image remain influenced by the preceding image. This indicates in some way the limit of the sensitivity of the present method. However, the present study shows that such Riemannian classification pipelines allow, on the one hand, scalp EEG signal discrimination throughout multiple subjects which could be used in an object visual recognition BCI and, on the other hand, EEG neural generators discrimination in a single subject which could be used in a clinical context. This latter aspect is in line with the present trend to favorize the decoding of the individual brain activity [63], [64] which outperforms the use of the grand average from multiple subjects.

We are also aware that the presented results are directed towards the global aspect of the visual image, though the two different images presented different physical characteristics (bottom-up features such as luminescence and contrast) and different representational contents (top-down influence). The distinctive influence of these physical and neuro-cognitive factors on the Riemannian classification pipelines will be further investigated. Future research could also be oriented towards new stimulation paradigms in order to differentiate EEG signals evoked by images with similar physical characteristics but different representational contents. Besides, in order to better understand the fundamental underlying neurophysiological mechanisms, future research may also be dedicated to quantify the importance of the discriminative patterns identified by the Riemannian classification pipelines.

5 Conclusion

This work shows that classification pipelines based on Riemannian geometry can effectively discriminate between the display of different visual items (Checkerboard versus 3D navigational image) in single EEG trials. The presented methodology reaches a single-trial classification accuracy of about 84% and 93% for inter-subject and intra-subject classification respectively using surface EEG. Furthermore, the classification algorithms trained on sLORETA estimation fail to generalize among multiple subjects (68% accuracy) but reach an intra-subject classification accuracy of 86% which allows future functional links between neuro-imagery and EEG dynamics discrimination. In this context, the development of new advanced mathematical frameworks will be paramount to develop a deeper understanding of the underlying communicational dynamics inside the neural network topography upon which the Riemannian classification pipeline performances emerged.

6 Acknowledgment

7 References

[1] S. Kurita-Tashima, S. Tobimatsu, M. Nakayama-Hiromatsu, and M. Kato, "Effect of check size on the pattern reversal visual evoked potential," *Electroencephalogr. Clin. Neurophysiol.*, vol. 80, no. 3, pp. 161–166, Jun. 1991, doi: 10.1016/0168-5597(91)90118-h.

[2] G. Cheron *et al.*, "Gravity influences top-down signals in visual processing," *PloS One*, vol. 9, no. 1, p. e82371, 2014, doi: 10.1371/journal.pone.0082371.

[3] Y. Shigihara, H. Hoshi, and S. Zeki, "Early visual cortical responses produced by checkerboard pattern stimulation," *NeuroImage*, vol. 134, pp. 532–539, 01 2016, doi: 10.1016/j.neuroimage.2016.03.078.

[4] F. Di Russo, A. Martínez, M. I. Sereno, S. Pitzalis, and S. A. Hillyard, "Cortical sources of the early components of the visual evoked potential," *Hum. Brain Mapp.*, vol. 15, no. 2, pp. 95–111, Feb. 2002.

[5] B. Rossion and S. Caharel, "ERP evidence for the speed of face categorization in the human brain: Disentangling the contribution of low-level visual cues from face perception," *Vision Res.*, vol. 51, no. 12, pp. 1297–1311, Jun. 2011, doi: 10.1016/j.visres.2011.04.003.

[6] S. Baijot *et al.*, "EEG Dynamics of a Go/Nogo Task in Children with ADHD," *Brain Sci.*, vol. 7, no. 12, Dec. 2017, doi: 10.3390/brainsci7120167.

[7] A. Leroy, C. Cevallos, A.-M. Cebolla, S. Caharel, B. Dan, and G. Cheron, "Short-term EEG dynamics and neural generators evoked by navigational images," *PloS One*, vol. 12, no. 6, p. e0178817, 2017, doi: 10.1371/journal.pone.0178817.

[8] S. J. E. Langeslag and J. W. van Strien, "Early visual processing of snakes and angry faces: An ERP study," *Brain Res.*, vol. 1678, pp. 297–303, Jan. 2018, doi: 10.1016/j.brainres.2017.10.031.

[9] S. Makeig *et al.*, "Dynamic brain sources of visual evoked responses," *Science*, vol. 295, no. 5555, pp. 690–694, Jan. 2002, doi: 10.1126/science.1066168.

[10] S. Hanslmayr *et al.*, "Alpha phase reset contributes to the generation of ERPs," *Cereb. Cortex N. Y. N 1991*, vol. 17, no. 1, pp. 1–8, Jan. 2007, doi: 10.1093/cercor/bhj129.

[11] P. Sauseng and W. Klimesch, "What does phase information of oscillatory brain activity tell us about cognitive processes?," *Neurosci. Biobehav. Rev.*, vol. 32, no. 5, pp. 1001–1013, Jul. 2008, doi: 10.1016/j.neubiorev.2008.03.014.

[12] R. Freunberger, R. Fellinger, P. Sauseng, W. Gruber, and W. Klimesch, "Dissociation between phase-locked and nonphase-locked alpha oscillations in a working memory task," *Hum. Brain Mapp.*, vol. 30, no. 10, pp. 3417–3425, Oct. 2009, doi: 10.1002/hbm.20766.

[13] L. Iemi *et al.*, "Multiple mechanisms link prestimulus neural oscillations to sensory responses," *eLife*, vol. 8, Jun. 2019, doi: 10.7554/eLife.43620.

[14] G. Cheron *et al.*, "Pure phase-locking of beta/gamma oscillation contributes to the N30 frontal component of somatosensory evoked potentials," *BMC Neurosci.*, vol. 8, p. 75, Sep. 2007, doi: 10.1186/1471-2202-8-75.

[15] A. Delorme, M. Miyakoshi, T.-P. Jung, and S. Makeig, "Grand average ERP-image plotting and statistics: A method for comparing variability in event-related single-trial EEG activities across subjects and conditions," *J. Neurosci. Methods*, vol. 250, pp. 3–6, Jul. 2015, doi: 10.1016/j.jneumeth.2014.10.003.

[16] E. S. Kappenman and S. J. Luck, "Best Practices for Event-Related Potential Research in Clinical Populations," *Biol. Psychiatry Cogn. Neurosci. Neuroimaging*, vol. 1, no. 2, pp. 110–115, Mar. 2016, doi: 10.1016/j.bpsc.2015.11.007.

[17] R. D. Pascual-Marqui, "Standardized low-resolution brain electromagnetic tomography (sLORETA): technical details," *Methods Find. Exp. Clin. Pharmacol.*, vol. 24 Suppl D, pp. 5–12, 2002.

[18] E. Palmero-Soler, K. Dolan, V. Hadamschek, and P. A. Tass, "swLORETA: a novel approach to robust source localization and synchronization tomography," *Phys. Med. Biol.*, vol. 52, no. 7, pp. 1783–1800, Apr. 2007, doi: 10.1088/0031-9155/52/7/002.

[19] A. M. Cebolla, E. Palmero-Soler, B. Dan, and G. Cheron, "Frontal phasic and oscillatory generators of the N30 somatosensory evoked potential," *NeuroImage*, vol. 54, no. 2, pp. 1297–1306, Jan. 2011, doi: 10.1016/j.neuroimage.2010.08.060.

[20] A.-M. Cebolla, E. Palmero-Soler, A. Leroy, and G. Cheron, "EEG Spectral Generators Involved in Motor Imagery: A swLORETA Study," *Front. Psychol.*, vol. 8, p. 2133, 2017, doi: 10.3389/fpsyg.2017.02133.

[21] A. Leroy *et al.*, "EEG Dynamics and Neural Generators in Implicit Navigational Image Processing in Adults with ADHD," *Neuroscience*, Jan. 2018, doi: 10.1016/j.neuroscience.2018.01.022.

[22] F. Lotte, M. Congedo, A. Lécuyer, F. Lamarche, and B. Arnaldi, "A review of classification algorithms for EEG-based brain-computer interfaces," *J. Neural Eng.*, vol. 4, no. 2, pp. R1–R13, Jun. 2007, doi: 10.1088/1741-2560/4/2/R01.

[23] B. Rivet, A. Souloumiac, V. Attina, and G. Gibert, "xDAWN algorithm to enhance evoked potentials: application to brain-computer interface," *IEEE Trans. Biomed. Eng.*, vol. 56, no. 8, pp. 2035–2043, Aug. 2009, doi: 10.1109/TBME.2009.2012869.

[24] A. Barachant, S. Bonnet, M. Congedo, and C. Jutten, "Multiclass brain-computer interface classification by Riemannian geometry," *IEEE Trans. Biomed. Eng.*, vol. 59, no. 4, pp. 920–928, Apr. 2012, doi: 10.1109/TBME.2011.2172210.

[25] H. Cecotti and A. J. Ries, "Best practice for single-trial detection of event-related potentials: Application to brain-computer interfaces," *Int. J. Psychophysiol. Off. J. Int. Organ. Psychophysiol.*, vol. 111, pp. 156–169, 2017, doi: 10.1016/j.ijpsycho.2016.07.500.

[26] F. Yger, M. Berar, and F. Lotte, "Riemannian Approaches in Brain-Computer Interfaces: A Review," *IEEE Trans. Neural Syst. Rehabil. Eng. Publ. IEEE Eng. Med. Biol. Soc.*, vol. 25, no. 10, pp. 1753–1762, 2017, doi: 10.1109/TNSRE.2016.2627016.

[27] J. Wang, Z. Feng, N. Lu, and J. Luo, "Toward optimal feature and time segment selection by divergence method for EEG signals classification," *Comput. Biol. Med.*, vol. 97, pp. 161–170, 01 2018, doi: 10.1016/j.compbiomed.2018.04.022.

[28] S. Blum, N. S. J. Jacobsen, M. G. Bleichner, and S. Debener, "A Riemannian Modification of Artifact Subspace Reconstruction for EEG Artifact Handling," *Front. Hum. Neurosci.*, vol. 13, p. 141, 2019, doi: 10.3389/fnhum.2019.00141.

[29] S. Chevallier, E. K. Kalunga, Q. Barthélemy, and E. Monacelli, "Review of Riemannian Distances and Divergences, Applied to SSVEP-based BCI," *Neuroinformatics*, Jun. 2020, doi: 10.1007/s12021-020-09473-9.

[30] J. Xu, M. Grosse-Wentrup, and V. Jayaram, "Tangent space spatial filters for interpretable and efficient Riemannian classification," *J. Neural Eng.*, vol. 17, no. 2, p. 026043, May 2020, doi: 10.1088/1741-2552/ab839e.

[31] H. Zeng and A. Song, "Optimizing Single-Trial EEG Classification by Stationary Matrix Logistic Regression in Brain–Computer Interface," *IEEE Trans. Neural Netw. Learn. Syst.*, vol. 27, no. 11, pp. 2301–2313, Nov. 2016, doi: 10.1109/TNNLS.2015.2475618.

[32] F. Lotte *et al.*, "A review of classification algorithms for EEG-based brain-computer interfaces: a 10 year update," *J. Neural Eng.*, vol. 15, no. 3, p. 031005, 2018, doi: 10.1088/1741-2552/aab2f2.

[33] M. Congedo, P. L. C. Rodrigues, F. Bouchard, A. Barachant, and C. Jutten, "A closed-form unsupervised geometry-aware dimensionality reduction method in the Riemannian Manifold of SPD matrices," *Conf. Proc. Annu. Int. Conf. IEEE Eng. Med. Biol. Soc. IEEE Eng. Med. Biol. Soc. Annu. Conf.*, vol. 2017, pp. 3198–3201, 2017, doi: 10.1109/EMBC.2017.8037537.

[34] M. Vidal, M.-A. Amorim, and A. Berthoz, "Navigating in a virtual three-dimensional maze: how do egocentric and allocentric reference frames interact?," *Brain Res. Cogn. Brain Res.*, vol. 19, no. 3, pp. 244–258, May 2004, doi: 10.1016/j.cogbrainres.2003.12.006.

[35] A. Delorme and S. Makeig, "EEGLAB: an open source toolbox for analysis of single-trial EEG dynamics including independent component analysis," *J. Neurosci. Methods*, vol. 134, no. 1, pp. 9–21, Mar. 2004, doi: 10.1016/j.jneumeth.2003.10.009.

[36] Barachant A, "MEG decoding using Riemannian geometry and unsupervised classification." 2014.

[37] O. Ledoit and M. Wolf, "A well-conditioned estimator for large-dimensional covariance matrices," *J. Multivar. Anal.*, vol. 88, no. 2, pp. 365–411, 2004.

[38] Y. Chen, A. Wiesel, Y. C. Eldar, and A. O. Hero, "Shrinkage Algorithms for MMSE Covariance Estimation," *IEEE Trans. Signal Process.*, vol. 58, no. 10, pp. 5016–5029, Oct. 2010, doi: 10.1109/TSP.2010.2053029.

[39] M. Moakher, "A Differential Geometric Approach to the Geometric Mean of Symmetric Positive-Definite Matrices," *SIAM J Matrix Anal. Appl.*, vol. 26, pp. 735–747, Jan. 2005, doi: 10.1137/S0895479803436937.

[40] O. Tuzel, F. Porikli, and P. Meer, "Pedestrian Detection via Classification on Riemannian Manifolds," *IEEE Trans. Pattern Anal. Mach. Intell.*, vol. 30, no. 10, pp. 1713–1727, Oct. 2008, doi: 10.1109/TPAMI.2008.75.

[41] A. Barachant, S. Bonnet, M. Congedo, and C. Jutten, "Classification of covariance matrices using a Riemannian-based kernel for BCI applications," *Neurocomputing*, vol. 112, pp. 172–178, Jul. 2013, doi: 10.1016/j.neucom.2012.12.039.

[42] R. D. Pascual-Marqui, C. M. Michel, and D. Lehmann, "Low resolution electromagnetic tomography: a new method for localizing electrical activity in the brain," *Int. J. Psychophysiol. Off. J. Int. Organ. Psychophysiol.*, vol. 18, no. 1, pp. 49–65, Oct. 1994, doi: 10.1016/0167-8760(84)90014-x.

[43] A. Gramfort *et al.*, "MNE software for processing MEG and EEG data," *NeuroImage*, vol. 86, pp. 446–460, Feb. 2014, doi: 10.1016/j.neuroimage.2013.10.027.

[44] R. S. Desikan *et al.*, "An automated labeling system for subdividing the human cerebral cortex on MRI scans into gyral based regions of interest," *NeuroImage*, vol. 31, no. 3, pp. 968–980, Jul. 2006, doi: 10.1016/j.neuroimage.2006.01.021.

[45] O. Potvin, L. Dieumegarde, S. Duchesne, and Alzheimer's Disease Neuroimaging Initiative, "Freesurfer cortical normative data for adults using Desikan-Killiany-Tourville and ex vivo protocols," *NeuroImage*, vol. 156, pp. 43–64, 01 2017, doi: 10.1016/j.neuroimage.2017.04.035.

[46] A. Gramfort *et al.*, "MEG and EEG data analysis with MNE-Python," *Front. Neurosci.*, vol. 7, 2013, doi: 10.3389/fnins.2013.00267.

[47] C. R. Harris *et al.*, "Array programming with NumPy," *Nature*, vol. 585, no. 7825, Art. no. 7825, Sep. 2020, doi: 10.1038/s41586-020-2649-2.

[48] E. Jones, T. Oliphant, and P. Peterson, "SciPy: Open Source Scientific Tools for Python," Jan. 2001.

[49] F. Pedregosa *et al.*, "Scikit-learn: Machine Learning in Python," *J. Mach. Learn. Res.*, vol. 12, Jan. 2012.

[50] A. Barachant and S. Bonnet, "Channel selection procedure using riemannian distance for BCI applications," in *2011 5th International IEEE/EMBS Conference on Neural Engineering*, Cancun, Apr. 2011, pp. 348–351, doi: 10.1109/NER.2011.5910558.

[51] J. R. Wolpaw *et al.*, "Brain-computer interface technology: a review of the first international meeting," *IEEE Trans. Rehabil. Eng. Publ. IEEE Eng. Med. Biol. Soc.*, vol. 8, no. 2, pp. 164–173, Jun. 2000.

[52] J. R. Wolpaw, N. Birbaumer, D. J. McFarland, G. Pfurtscheller, and T. M. Vaughan, "Brain-computer interfaces for communication and control," *Clin. Neurophysiol. Off. J. Int. Fed. Clin. Neurophysiol.*, vol. 113, no. 6, pp. 767–791, Jun. 2002, doi: 10.1016/s1388-2457(02)00057-3.

[53] C. Tomberg and J. E. Desmedt, "A method for identifying short-latency human cognitive potentials in single trials by scalp mapping," *Neurosci. Lett.*, vol. 168, no. 1–2, pp. 123–125, Feb. 1994, doi: 10.1016/0304-3940(94)90431-6.

[54] C. Tomberg and J. E. Desmedt, "Non-averaged human brain potentials in somatic attention: the short-latency cognition-related P40 component," *J. Physiol.*, vol. 496 (Pt 2), pp. 559–574, Oct. 1996, doi: 10.1113/jphysiol.1996.sp021707.

[55] W. G. Coon and G. Schalk, "A method to establish the spatiotemporal evolution of task-related cortical activity from electrocorticographic signals in single trials," *J. Neurosci. Methods*, vol. 271, pp. 76–85, Sep. 2016, doi: 10.1016/j.jneumeth.2016.06.024.

[56] H. G. Rey, M. Ahmadi, and R. Quian Quiroga, "Single trial analysis of field potentials in perception, learning and memory," *Curr. Opin. Neurobiol.*, vol. 31, pp. 148–155, Apr. 2015, doi: 10.1016/j.conb.2014.10.009.

[57] F. P. Kalaganis, N. A. Laskaris, E. Chatzilari, S. Nikolopoulos, and I. Kompatsiaris, "A Riemannian Geometry Approach to Reduced and Discriminative Covariance Estimation in Brain Computer Interfaces," *IEEE Trans. Biomed. Eng.*, vol. 67, no. 1, pp. 245–255, Jan. 2020, doi: 10.1109/TBME.2019.2912066.

[58] A. X. Stewart, A. Nuthmann, and G. Sanguinetti, "Single-trial classification of EEG in a visual object task using ICA and machine learning," *J. Neurosci. Methods*, vol. 228, pp. 1–14, May 2014, doi: 10.1016/j.jneumeth.2014.02.014.

[59] S. Guan, K. Zhao, and S. Yang, "Motor Imagery EEG Classification Based on Decision Tree Framework and Riemannian Geometry," *Computational Intelligence and Neuroscience*, Jan. 21, 2019. https://www.hindawi.com/journals/cin/2019/5627156/ (accessed Aug. 03, 2020).

[60] I. Majidov and T. Whangbo, "Efficient Classification of Motor Imagery Electroencephalography Signals Using Deep Learning Methods," *Sensors*, vol. 19, no. 7, Art. no. 7, Jan. 2019, doi: 10.3390/s19071736.

[61] L. Korczowski, M. Congedo, and C. Jutten, "Single-trial classification of multi-user P300-based Brain-Computer Interface using riemannian geometry," in *2015 37th Annual International Conference of the IEEE Engineering in Medicine and Biology Society (EMBC)*, Aug. 2015, pp. 1769–1772, doi: 10.1109/EMBC.2015.7318721.

[62] X. Navarro-Sune *et al.*, "Riemannian Geometry Applied to Detection of Respiratory States From EEG Signals: The Basis for a Brain-Ventilator Interface," *IEEE Trans. Biomed. Eng.*, vol. 64, no. 5, pp. 1138–1148, 2017, doi: 10.1109/TBME.2016.2592820.

[63] J. D. Karch, M. C. Sander, T. von Oertzen, A. M. Brandmaier, and M. Werkle-Bergner, "Using within-subject pattern classification to understand lifespan age differences in oscillatory

mechanisms of working memory selection and maintenance," *NeuroImage*, vol. 118, pp. 538–552, 2015, doi: 10.1016/j.neuroimage.2015.04.038.

[64] A. Leroy and G. Cheron, "EEG dynamics and neural generators of psychological flow during one tightrope performance," *Sci. Rep.*, vol. 10, no. 1, Art. no. 1, Jul. 2020, doi: 10.1038/s41598-020-69448-3.